TU Delft

Delft University of Technology

Document Version
Final published version

Licence
Dutch Copyright Act (Article 25fa)

Citation (APA)
Qu, B., Ni, J., Huang, C., Ding, J., Zhou, R., Zhu, C., Wang, L., & Hintzen, H. T. (2026). Dual-crystal-field luminescence in Fe3+-Doped Sr4Al14O25for high-sensitivity near-infrared thermometry and anti-counterfeiting. *Ceramics International*, *52*(4), 5242-5250. https://doi.org/10.1016/j.ceramint.2025.12.297

Important note
To cite this publication, please use the final published version (if applicable).
Please check the document version above.

Copyright
In case the licence states “Dutch Copyright Act (Article 25fa)”, this publication was made available Green Open Access via the TU Delft Institutional Repository pursuant to Dutch Copyright Act (Article 25fa, the Taverne amendment). This provision does not affect copyright ownership.
Unless copyright is transferred by contract or statute, it remains with the copyright holder.

Sharing and reuse
Other than for strictly personal use, it is not permitted to download, forward or distribute the text or part of it, without the consent of the author(s) and/or copyright holder(s), unless the work is under an open content license such as Creative Commons.

Takedown policy
Please contact us and provide details if you believe this document breaches copyrights.
We will remove access to the work immediately and investigate your claim.

This work is downloaded from Delft University of Technology.

Ceramics International 52 (2026) 5242–5250

Contents lists available at ScienceDirect

Ceramics International

journal homepage: www.elsevier.com/locate/ceramint

Dual-crystal-field luminescence in Fe^{3+}-Doped $Sr_4Al_{14}O_{25}$ for high-sensitivity near-infrared thermometry and anti-counterfeiting

Bingyan Qu [a,d], Jindong Ni [a], Chenglan Huang [a], Junxiang Ding [a], Rulong Zhou [a], Caiping Zhu [c], Lei Wang [a,d,*], Hubertus T. Hintzen [b,**]

[a] School of Materials Science and Engineering, Hefei University of Technology, Hefei, 230009, Anhui, China
[b] Luminescent Materials Group, Delft University of Technology, Mekelweg 15, Delft, 2629 JB, Netherlands
[c] Henan Zhongyuan Expressway Co.,LTD, Zhengzhou, Henan, 450045, China
[d] Engineering Research Center of High Performance Copper Alloy Materials and Processing, Ministry of Education, Hefei University of Technology, Hefei, 230009, China

A B S T R A C T

Luminescence thermometry has emerged as a promising non-invasive technique for precise temperature measurement, particularly in fields such as microelectronics, optoelectronics, and biomedicine. Here, we report the development of a novel dual-mode near-infrared (NIR) luminescence thermometer based on Fe^{3+}-doped $Sr_4Al_{14}O_{25}$ (SAO). By integrating experimental and first-principles computational approaches, we demonstrate that Fe^{3+} ions occupy both tetrahedral and octahedral sites within the SAO host material, yielding distinct broad band emissions with peaks at 752 nm and 812 nm. The temperature-dependent fluorescence intensity ratio (FIR) of these emissions exhibits a maximum relative temperature sensitivity of 2.72 % K^{-1}, making this material a highly promising candidate for precision temperature sensing. Furthermore, the material's potential for application in anti-counterfeiting technologies is explored, suggesting its versatility in multifunctional optoelectronic devices. This work not only advances the understanding of Fe^{3+}-doped NIR emitting materials but also opens new avenues for their practical applications in diverse fields.

1. Introduction

Luminescence thermometry has recently garnered significant interest as a novel method for temperature measurement, offering non-invasive and spatially resolved readings as a viable alternative to conventional contact thermometers in various fields, including microelectronics, optoelectronics and biomedicine [1–3]. This technique exploits the temperature-dependent properties of luminescent materials, such as emission wavelength, excited state lifetime, and fluorescence intensity ratio (FIR) [1,4]. Among these properties, ratiometric thermometry, which utilizes the FIR of two separate emission peaks with distinct temperature sensitivities under the same excitation wavelength, has demonstrated precise sensing capabilities with relatively minimal measurement errors [2,5].

Notably, near-infrared (NIR) emissions are particularly valuable for temperature sensing, especially in biological environments, due to reduced autofluorescence and deeper tissue penetration. Materials like $LaPO_4$:Nd^{3+} [6] and $SrTiO_3$:Ni^{2+}, Er^{3+} [7] have enabled ultra-sensitive optical thermometers, aligning with the optical transparency window of biological tissues [3,8,9]. Consequently, NIR thermometric phosphors, characterized by high sensitivity, rapid response times, and broad adaptability, show great promise for practical applications. However, compared to numerous visible-region thermometric phosphors reported in literature and practice, NIR ones are relatively scarce.

This study focuses on Fe^{3+} ion, a prominent NIR activator [10–13], as it exhibits broad band emissions in the NIR range. Notably, the peak energy of the emission band from Fe^{3+} at a tetrahedral site is higher than that at an octahedral site [10,14]. Moreover, the ion's 3d orbitals extending outside and being susceptible to local environmental changes, the distinct peak energies and their different temperature dependence sensitivities at tetrahedral and octahedral sites might suggest the possibility of dual-mode NIR luminescence thermometry when it is integrated within a host material that supports both crystal fields simultaneously. Furthermore, unlike the narrow-line emissions typical of most trivalent lanthanide ions, the broad emission bands of Fe^{3+} has a wider range of adaptability to most high-precision temperature sensing equipment [15,16]. $Sr_4Al_{14}O_{25}$ (SAO), a wide-bandgap compound, is a promising host material for Fe^{3+} due to its ability to accommodate both tetrahedral and octahedral crystal fields and its efficient luminescence when doped with various ions, such as Mn^{4+} [17,18], Mn^{2+} [19] and

* Corresponding author. School of Materials Science and Engineering, Hefei University of Technology, Hefei, 230009, Anhui, China
** Corresponding Author. Luminescent Materials Group, Delft University of Technology, Mekelweg 15, Delft, 2629 JB, Netherlands
E-mail addresses: leiwang@hfut.edu.cn, leiw03@126.com (L. Wang), H.T.Hintzen@tudelft.nl (H.T. Hintzen).

https://doi.org/10.1016/j.ceramint.2025.12.297
Received 15 August 2025; Received in revised form 14 December 2025; Accepted 18 December 2025
Available online 19 December 2025
0272-8842/© 2025 Elsevier Ltd and Techna Group S.r.l. All rights are reserved, including those for text and data mining, AI training, and similar technologies.

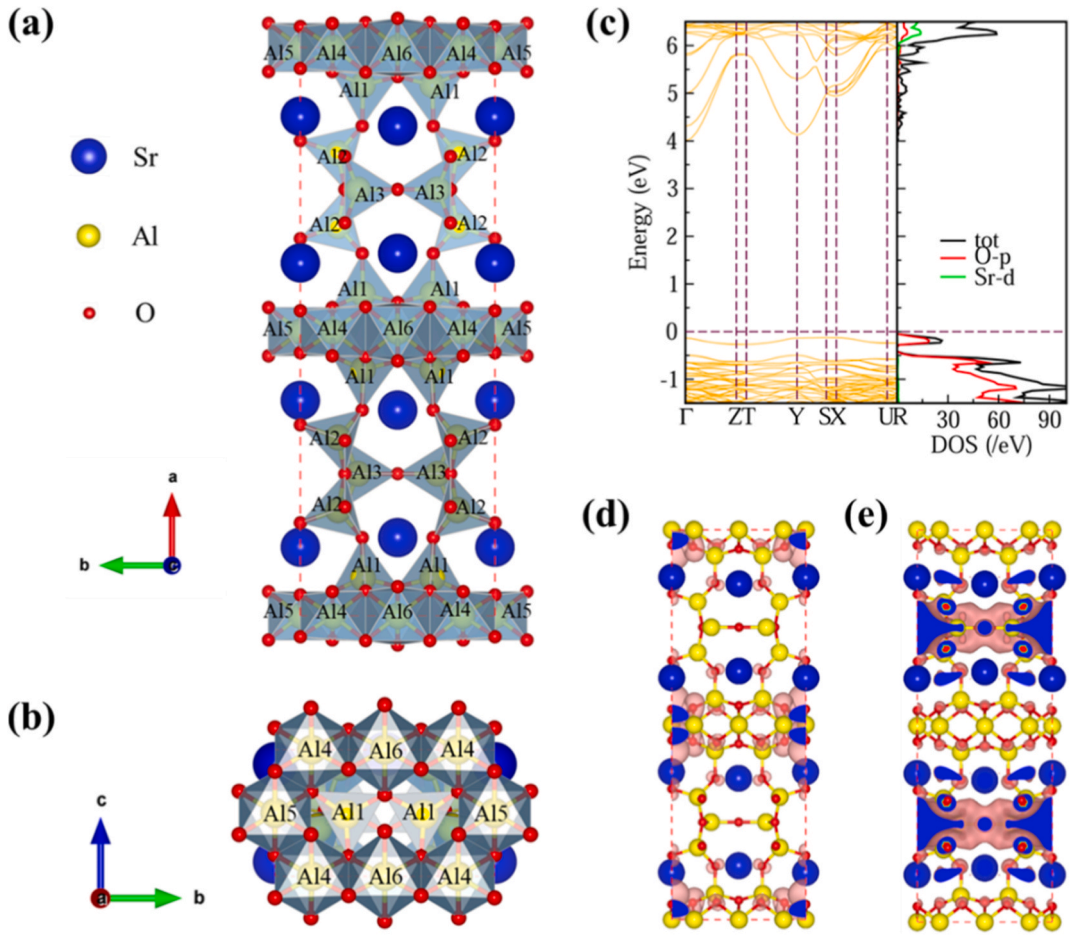


Fig. 1. (a) and (b) Crystal structure of SAO. (c) The electronic structure, total (tot) and projected (O-p, Sr-d) density of states of undoped SAO. The Fermi level is set to be 0 eV. The iso-surfaces of the charge densities of the top of valence band (d) and the bottom of conduction band (e).

Cr^{3+} [20].

Thus, this work investigates the luminescence properties of Fe^{3+} doped in SAO through both experimental and first-principles computational approaches. The results verify that Fe^{3+} can indeed occupy tetrahedral and octahedral Al^{3+} sites simultaneously in SAO, displaying broad emission bands in the NIR range, 752 nm for tetrahedral Fe^{3+} and 812 nm for octahedral Fe^{3+}. Interestingly, with increasing temperature the emission from tetrahedral site diminishes more quickly than that from octahedral site, highlighting the distinct temperature-sensitivities of Fe^{3+} at these two sites. Upon UV–VIS excitation, the relative temperature sensitivity S_r, estimated from the FIR of 752 and 812 nm peaks, reaches a maximum of 2.72 % K^{-1}, indicating promising application prospects in luminescence temperature measurement. This work expands the understanding of Fe^{3+}-doped NIR materials and motivates their potential for future applications.

2. Methods

2.1. First principles calculations

The distribution of Fe^{3+} among the Al^{3+} sites in SAO and the dopant levels induced by Fe^{3+} in the host band gap are studied using the VASP code within the framework of density functional theory [21,22]. The projector augmented wave (PAW) method with the cutoff of 400 eV and the GGA-PBE approximation were adopted [23]. To account for the strong correlations of Fe^{3+} 3d electrons, the GGA + U method was applied [24] and the influence of different U values on the defect levels of Fe^{3+} ion was discussed in the supplementary information (SI). A supercell containing 1 × 1 × 2 unit cells with one Al atom replaced by an Fe atom was used as the structural model and a 2 × 4 × 4 k-points mesh was adopted. All the calculations about the total energies and the band structures were carried out after the structural model fully-relaxed until the residual force on each ion less than 0.01 eV/Å. The formation energies of Fe^{3+} ($E_F(Fe^{3+})$) at different Al^{3+} sites was calculated by using the following equation [25]:

$$E_F(Fe^{3+}) = E(SAO : Fe^{3+}) - E(SAO) - \mu_{Fe} + \mu_{Al}, \quad (1)$$

where $E(SAO : Fe^{3+})$ and $E(SAO)$ are the total energies of SAO with and without Fe^{3+} ion, and μ_{Fe} and μ_{Al} represent the chemical potentials of bulk Fe and Al metal, respectively.

2.2. Sample preparation

A series of $Sr_4Al_{14(1-x)}Fe_{14x}O_{25}$ (SAO:$x$$Fe^{3+}$) samples with varying Fe^{3+} concentrations (x = 0, 0.1, 0.2, 0.3, 0.4, 0.5, 0.6, and 0.7 mol% of Al) were prepared by a high-temperature solid-state reaction method. Stoichiometric amounts of Al_2O_3 (99.99 %), $SrCO_3$ (99.99 %) and Fe_2O_3 (99.99 %) were mixed with 3 wt% H_3BO_3 as a sintering aid. The mixture was ground in an agate mortar, placed in an alumina crucible, and sintered in air at 1300 °C for 4 h. The samples were then reground into fine powder for characterization.

2.3. Characterization

X-ray diffraction (XRD) characterizations were performed using a PANalytical X-Pert PRO MPD diffractometer, with a step size of 0.02°

Table 1
The formation energies (eV) of Fe^{3+} occupying different Al sites.

Al1	Al2	Al3	Al4	Al5	Al6
0	0.09	0.09	0.21	0.39	0.17

and a counting time of 0.15 s per step for Cu Kα radiation (V = 40 kV, I = 40 mA). Scanning electron microscopy (SEM) images were obtained using a Hitachi Regulus instrument to assess the morphology of the synthesized powders. Energy dispersive spectroscopy (EDS) was conducted with detectors connected to the SEM, to confirm the elemental composition and distribution of Fe^{3+} within the SAO host material. Diffuse reflectance spectra (DRS) were collected using an UV–vis–NIR spectrophotometer (Agilent Cary-5000) to evaluate the optical absorption properties of the samples. The excitation and emission spectra of the samples were measured with a Hitachi F-4600 fluorescence spectrophotometer. Photoluminescence decay curves were recorded with a Horiba JY Fluorolog-3-tau steady-state/lifetime spectrofluorometer.

3. Results and discussion

3.1. Crystal structure and occupation of Fe^{3+}

$Sr_4Al_{14}O_{25}$ (SAO) belongs to the *Pmma* space group, and its crystal structure is shown in Fig. 1(a). According to the local coordination environments, the Al^{3+} ions in SAO occupy six non-identical sites, labeled as Al1, Al2, Al3, Al4, Al5 and Al6, which are marked in Fig. 1(a). The latter three Al sites (Al4, Al5 and Al6) are octahedrally coordinated, and these AlO_6 octahedrons construct layers in the ***ab***-plane by the vertex-sharing O^{2-} ions (Fig. 1(b)). Al1, Al2 and Al3 are bonded with four O^{2-} ions tetrahedrally and located between the AlO_6 layers. The detailed local coordinated environments of Al are listed in Table S1 of the supplementary information (SI). The Sr^{2+} ions are distributed in the interstitial sites among the AlO_6 and AlO_4 polyhedrons. Considering the ionic radius of Al^{3+} ion (0.39/0.535 Å) is slightly smaller than that of Fe^{3+} (0.49/0.645 Å) [26] in the tetrahedral/octahedral site, the rigid crystal structure and multi-type crystal fields of SAO offer a perfect host material for Fe^{3+} doping, which may achieve multiple luminescence with different temperature-sensitivities.

To test this speculation, we should make clear that Fe^{3+} ion can occupy the Al^{3+} sites with both types of crystal fields. The formation energy of Fe^{3+} ion at different Al^{3+} sites was calculated and listed in Table 1, where the lowest formation energy serves as the reference. Fe^{3+} ion at tetrahedral Al1 site has the lowest formation energy. The formation energies at other Al sites are very close to that at Al1, except at the Al5 site, indicating that Fe^{3+} ions can distribute across both types of crystal fields in SAO with a preference for the tetrahedral sites. The significantly higher formation energy for the Al5 octahedral site can be attributed to its distinct local structure. As listed in Table S1 (SI), the Al5-O bonds are the shortest among the AlO_6 octahedral. Substituting the smaller Al^{3+} with the larger Fe^{3+} at this compact site introduces considerable local strain, making the substitution energetically less favorable compared to other sites.

3.2. Dopant levels induced by Fe^{3+}

Subsequently, we investigate the electronic structures of SAO without and with Fe^{3+} ions. The electronic structure of undoped SAO is shown in Fig. 1(c). The calculated band gap is approximately 4.1 eV, which is about 2.4 eV lower than the experimental value of about 6.5 eV [27]. This discrepancy is attributed to the GGA-PBE method, which typically underestimates the band gaps for insulator materials. As illustrated by the density of the states (DOS), the valence band of SAO is primarily formed through the hybridization of the 2p orbitals of O^{2-} ions. Notably, the charge density of the top of the valence band predominantly resides around the O^{2-} ions that surround octahedral Al5 sites as depicted in Fig. 1(d). This leads to the formation of one-dimensional isolated chains along the ***a***-axis. Conversely, the charge density of the bottom of the conduction band (Fig. 1(e)) is mainly localized within the Al2 and Al3 tetrahedrons layers (the density of states of Al are too smaller and not shown in Fig. 1(c)). It is evident that the wavefunctions of the top of valence band and the bottom of conduction band have distinct spatial locations within the crystal. The band edge absorption involves the electron transitioning from the O^{2-} ions of the AlO6 octahedron to the orbitals of AlO4 tetrahedron. Furthermore, the contribution of Sr-d orbitals within the conduction band is apparent in the energy range near 6 eV, as depicted in Fig. 1(c).

The electronic structure of SAO with Fe^{3+} occupying each Al site is calculated and the ones with Fe at tetrahedral Al1 and octahedral Al4 site are illustrated in Fig. 2(a and b) representatively. In comparison to undoped SAO, the 3d orbitals of Fe^{3+} at the Al1 site induce the dopant levels (denoted as blue curves), manifesting both the spin up and spin down states, in the band gap. These dopant levels correspond to antibonding orbitals formed between the 3d orbitals of Fe^{3+} and the 2p orbitals of O^{2-} ions (more discussion about the origin of the dopant levels of 3d ions can be found in Refs. [28,29]). The splitting energy of the 3d orbitals of Fe^{3+} at Al1 site is estimated from the spin down triplet and doublet states, which is approximately 0.8 eV. In contrast, the energy difference between the spin-down doublet states and spin up triplet states is around 1.6 eV. Given that the Fe^{3+} ion contains five 3d electrons and experiences week crystal field at both the tetrahedral and octahedral sites, the spin up states are fully occupied, corresponding to the ground state of Fe^{3+} ($^6A_1(^6S)$). Upon excitation, an electron from the spin up states transitions to one of the spin down states. After full relaxation, this

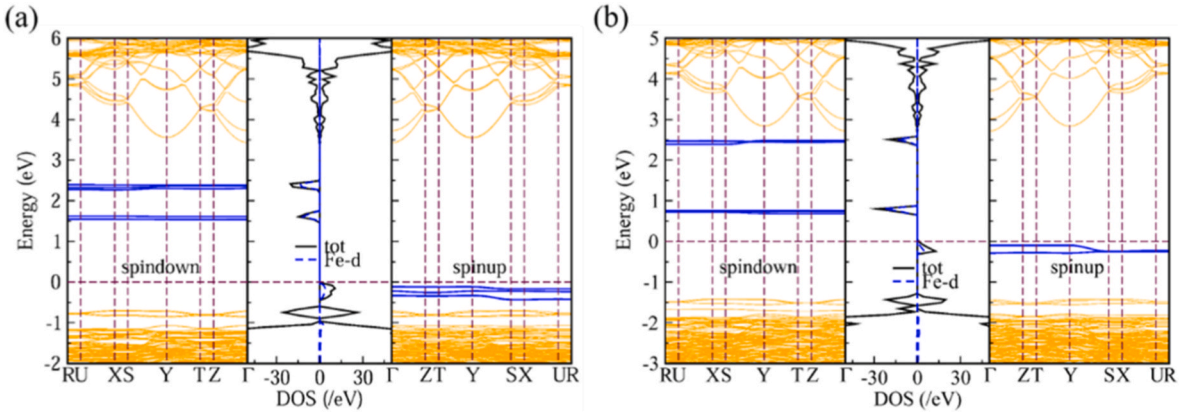


Fig. 2. The electronic structure, total (tot) and projected (O-p, Fe-d) density of states of SAO with Fe^{3+} occupying Al1 (a) and Al4 site (b). The Fermi level is set to be 0 eV.

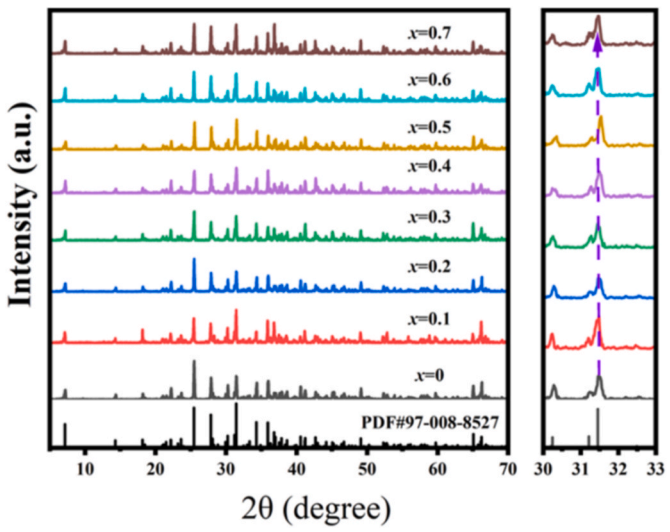


Fig. 3. The XRD patterns of SAO:xFe^{3+} and the enlarged XRD patterns in 2θ range of 30~33° on the right hand.

excited electron occupying the spin down doublet states, leaving one of the spin up triplet states unoccupied. When this excited electron returns to the empty state, near-infrared light is emitted. It is important to note that the spin up triplet states of the excited Fe^{3+} ions are not fully occupied, allowing them to accommodate electrons from the valence bands via thermal excitation. This is particularly relevant since the spin up triplet states are only about 0.5 eV above the valence band maximum (VBM), as illustrated in Fig. 2(a). This thermal excitation presents an unwanted mechanism that can interrupt the emission process of Fe^{3+} ions, particularly at elevated temperature. So, this process offers an additional non-radiative relaxation channel for the excited energy, alongside the intra-band relaxation within the 3d orbitals of Fe^{3+} [30].

As to the octahedral crystal field, Fe^{3+} ion can also induce dopant levels within the band gap, as illustrated in Fig. 2(b). These dopant levels primarily arise from the 3d orbitals of the Fe^{3+} ion. The spin up dopant levels are fully occupied, while the spin down dopant levels remain unfilled. The splitting energy between spin down triplet and doublet states of the Fe^{3+} ion in octahedral site is approximately 1.7 eV, which is larger than that experienced by Fe^{3+} in tetrahedral site, corresponding with stronger crystal field for octahedral versus tetrahedral site. The energy difference between the highest occupied dopant levels and the lowest empty dopant levels, which is directly related to the emission energy of Fe^{3+}, is about 0.8 eV and is lower than that at the tetrahedral site. This result qualitatively aligns with experimental observations, wherein the emission wavelength of Fe^{3+} in octahedral site is consistently longer than that in tetrahedral site [31,32]. A similar tendency (longer emission wavelength for stronger crystal field) has been observed in literature for the iso-electronic Mn^{2+} d^5 configuration [33]. As depicted in Fig. 2(b), the highest spin up dopant level is situated about 1.2 eV above the VBM, exceeding the corresponding level at the tetrahedral site. So, the nonradiative relaxation channel for the excited energy of Fe^{3+} from the valence band is expected to be less pronounced in the octahedral site than in tetrahedral site, suggesting enhanced thermal stability of the emission from octahedral Fe^{3+} ions.

To elucidate the predicted/calculated larger energy difference between the highest spin-up dopant level and the VBM of Fe^{3+} in the octahedral site as compared to the tetrahedral site, we consider the interaction of the 3d orbitals of Fe^{3+} with ligand orbitals, specifically the 2p orbitals of O^{2-}. The bonding orbitals have lower energy, while the

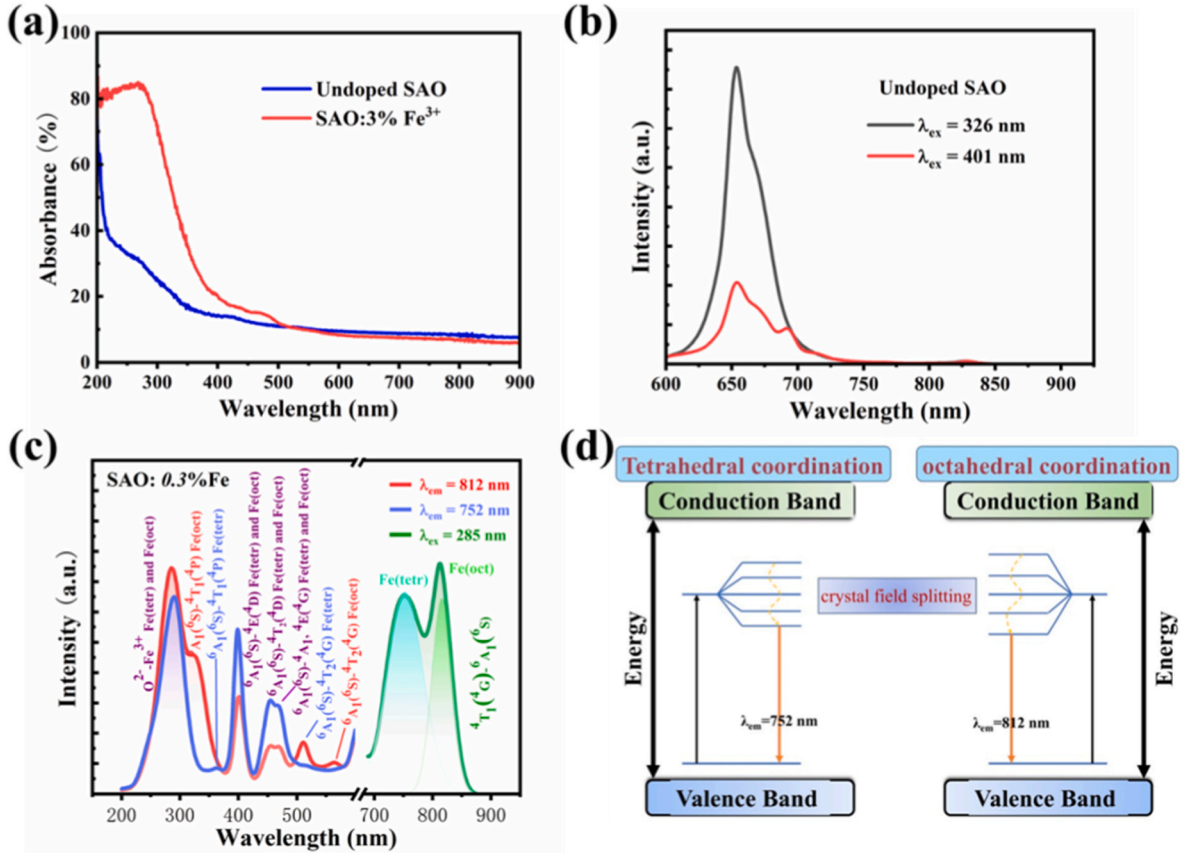


Fig. 4. (a) The DRS of SAO and SAO:0.3 %Fe^{3+}. (b) Emission spectra of the host SAO. (c) Excitation and emission spectra of SAO:0.3 %Fe^{3+}. (d) Schematic mechanism diagram of SAO:Fe^{3+} emission.

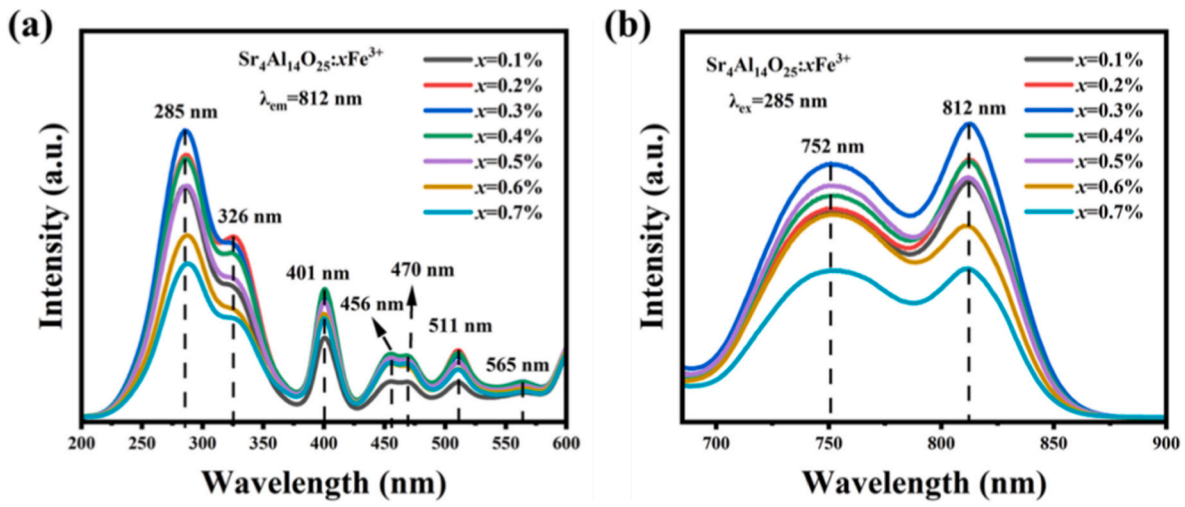


Fig. 5. (a) Excitation and (b) emission spectra of SAO:xFe^{3+} (x = 0.1–0.7 %).

antibonding orbitals possess higher energy, in between are the nonbonding orbitals, namely the 2p orbitals of O^{2-} not used for hybridization with Fe^{3+} d orbitals. When Fe-O polyhedron is situated within the host materials, the 2p orbitals of O^{2-} interact with each other and contribute to the formation of the valence band, as shown in Fig. 1. In comparing the octahedral and tetrahedral environments of Fe^{3+}, it is evident that the interaction between the 3d orbitals of Fe^{3+} and the 2p orbitals of O^{2-} is considerably stronger in the octahedral coordination due to enhanced orbital symmetry matching. This results in the higher energies for the antibonding orbitals (dopant levels) in the octahedral field.

In summary, the calculations indicate that Fe^{3+} ions can occupy both the tetrahedral and octahedral sites within SAO with the emission wavelength of Fe^{3+} at octahedral sites longer than that at tetrahedral sites. Notably, for Fe^{3+} ions coordinated in tetrahedral site, a higher temperature sensitivity is expected than for those coordinated octahedrally, positioning them as potential candidates for non-contact temperature sensing devices.

3.3. Phase identification and structure

To validate the predictions of our calculations, we synthesized a series of $Sr_4Al_{14(1-x)}Fe_{14x}O_{25}$ samples (SAO:xFe^{3+}) with varying Fe^{3+} concentration (x) from 0 to 0.7 % and measure their luminescence properties. Fig. 3 presents the XRD patterns of the synthesized samples SAO:xFe^{3+} (x = 0–0.7), along with the standard card PDF#97-008-8527 of undoped SAO. The peak positions of the undoped samples align well with those in the standard card. No impurity peaks are observed. Notably, the XRD patterns remain largely unchanged upon Fe^{3+} doping, as can be more clearly seen in the enlarged XRD patterns in the 2θ range of 30–33° shown on the right hand of Fig. 3. Considering the ionic radii and charge states, it is reasonable to conclude that the Fe^{3+} ions populate both tetrahedral and octahedral Al sites rather than Sr^{2+} sites. The SEM, EDS and elemental mapping images of the sample SAO:0.3 %Fe^{3+} exhibit that the sample consists of irregular-shaped particles with a size of tens of micrometers and confirm the presence of Fe^{3+} ions in the host lattice uniformly. More details are shown in SI.

3.4. Luminescence properties of SAO:xFe^{3+}

The UV–visible–NIR Diffuse reflection spectrum (DRS) of SAO host material and SAO:0.3 %Fe^{3+} are shown in Fig. 4(a). The undoped SAO host material displays no discernible absorption band due to its large band gap of approximately 6.5 eV [27]. A weak absorption band in the range of 350–450 nm may originate from trace Mn^{4+} impurities, likely unintentionally induced through the raw material Al_2O_3, as evidenced by the emission spectrum under 326 nm excitation shown in Fig. 4(b). This emission spectrum features a narrow band peaking at about 655 nm, indicating the presence of Mn^{4+} in the sample [18]. Its emission is negligible under the 285 nm excitation central to this study and does not

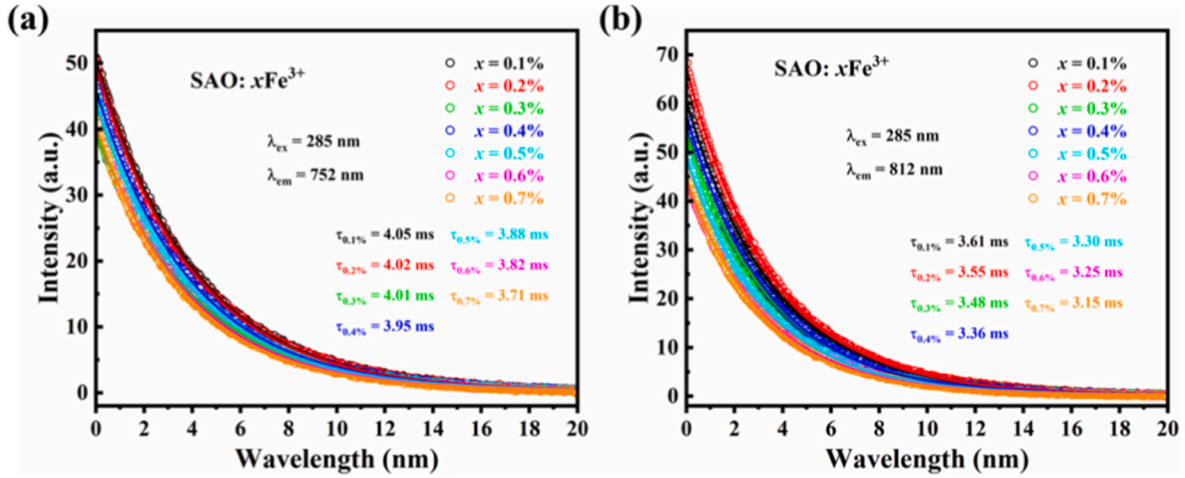


Fig. 6. Fluorescence attenuation curves of SAO:0.3 %Fe^{3+} at (a) 752 nm and (b) 812 nm.

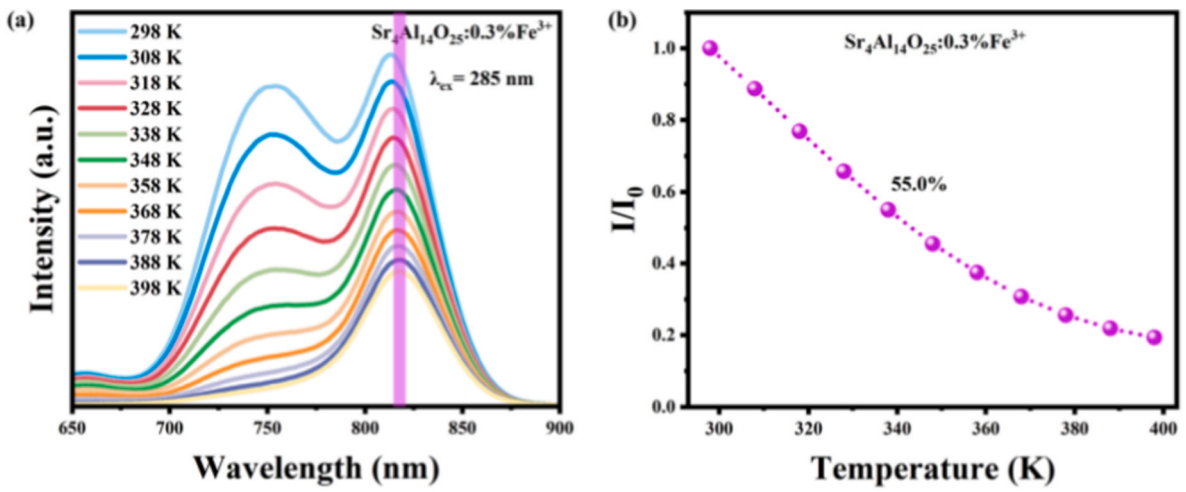


Fig. 7. (a) The temperature dependence of emission spectra for SAO:0.3 %Fe^{3+} at 298–398 K. (b) The variation of the integral emission intensity of SAO:0.3 %Fe^{3+} as a function of temperature, taking the integral emission intensity at 298 K as reference.

affect the primary NIR emissions from Fe^{3+} (see Fig. 9) or the thermometric analysis. The doping of Fe^{3+} ions in SAO induces additional absorption bands in the range of 250–350 nm and 400–500 nm, which can be attributed to the charge transfer transition from O^{2-} to Fe^{3+} and the d-d transitions within the 3d orbitals of Fe^{3+}, respectively. Similar observations have been reported in the literature [34,35].

The excitation and emission spectra of SAO:0.3 %Fe^{3+} are provided in Fig. 4(c). Under 285 nm excitation, two near-infrared emission peaks are observed at 752 nm and 812 nm, which are overlapping in the range of 700~870 nm. These emission peaks correspond to the $^4T_1(^4G)\rightarrow{}^6A_1(^6S)$ transitions of Fe^{3+}. The stronger crystal field of octahedral site results in longer wavelength emission, thus, the 812 nm emission can be reasonably assigned to the Fe^{3+} ions at octahedral sites (denoted as Fe(oct)), while the 752 nm peak corresponds to tetrahedral coordinated Fe^{3+} (Fe(tetr)). For the excitation spectrum, monitoring at either 812 nm or 752 nm reveals that the excitation bands cover a wide range from 200 to 600 nm, enhancing the light availability for excitation. The primary excitation peak at 285 nm is associated with the charge transfer (CT) transition from O^{2-} ions to Fe^{3+} ions at both tetrahedral and octahedral sites. The narrower peaks originate from the d-d transitions of Fe(tetr) and/or Fe(oct), as indicated in Fig. 4(c).

Fig. 5(a, b) present the excitation and emission spectra of samples with Fe^{3+} doping concentration ranging from 0.1 %–0.7 %. The emission increases synchronously, reaching the maximum value at an Fe^{3+} concentration of 0.3 %. With further increases in Fe^{3+} concentration, the excitation and emission intensities decrease monotonically, demonstrating concentration quenching behavior.

The luminescence decay curves of the emission peaks at 752 and 812 nm of SAO:$x$$Fe^{3+}$ (x = 0.1 %–0.7 %) under 285 nm excitation are collected in Fig. 6(a and b). Those curves can be well fitted using the following exponential decay formula [36]:

$$I = A_1 \exp\left(\frac{-t}{\tau}\right) + A_0 \quad (2)$$

where I represents luminescent intensity at time t, A_1 and A_0 are the corresponding constants. The obtained lifetimes τ for both the 752 nm and 812 nm emission peaks range from 3.15 ms to 4.05 ms, which are consistent with previously reported values for Fe^{3+}-activated materials [11,34]. In more details, the average lifetimes of both 752 and 812 nm decrease with Fe^{3+} concentration, likely due to enhanced energy transfer between Fe^{3+} ions at higher concentrations.

To evaluate the thermal stability of the emission from SAO:0.3 % Fe^{3+}, we investigated the variable temperature emission spectra over the range of 298–398 K. As illustrated in Fig. 7, the emission intensity of SAO:0.3 %Fe^{3+} decreases steadily with increasing temperature. Notably, at 338 K, the integral emission intensity is only 55.0 % of that observed at 298 K, demonstrating significant thermal quenching. It is particularly noteworthy that the intensity of the emission peak at 752 nm decays much more rapidly than that of the 812 nm peak. Specifically, at 398 K, the 752 nm peak nearly disappears, whereas the 812 nm peak retains approximately one-third of its intensity at 298 K. This observation highlights the distinctly different temperature sensitivities

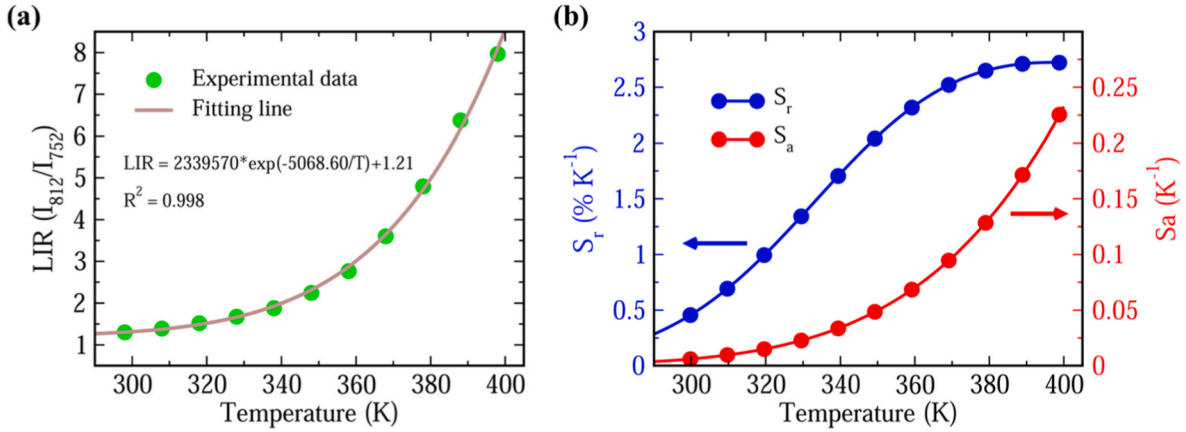
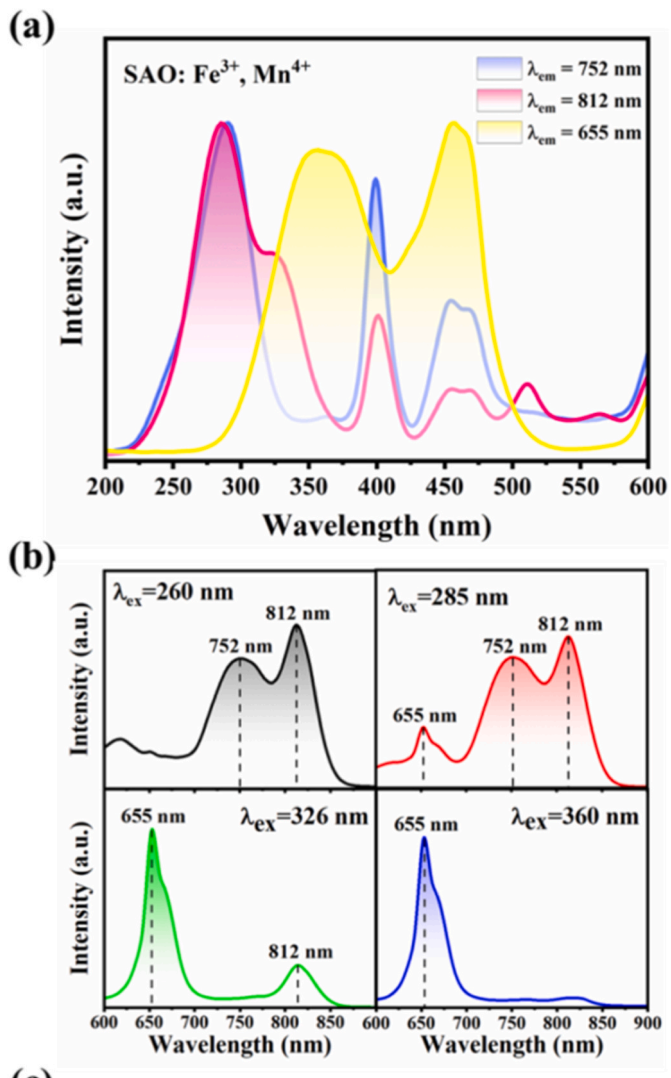


Fig. 8. (a) LIR and (b) corresponding absolute sensitivity S_a and relative sensitivity S_r at different temperatures.



(c)

Excitation	655 nm	752 nm	812 nm
260 nm	0	2	3
285 nm	1	2	3
326 nm	1	0	3
360 nm	1	0	0

Fig. 9. (a) The excitation spectra of SAO:Fe^{3+}, Mn^{4+} monitored at 752, 812 and 655 nm. (b) Emission spectra of SAO:Fe^{3+},Mn^{4+} phosphor excited at 260, 285, 326 and 360 nm and (c) the corresponding coding and decoding method.

of these two emissions. These findings align perfectly with our theoretical predictions that Fe^{3+}(tetr) emission shows a stronger temperature dependence as compared to Fe^{3+}(oct) emission as discussed earlier, further supporting the potential application of SAO:Fe^{3+} samples in non-contact temperature sensing devices.

3.5. Temperature response of SAO:Fe^{3+}

The luminescence intensity ratio (LIR) temperature measurement method utilizes phosphors with two emission peaks that exhibit different temperature sensitivities, garnering significant attention due to its excellent accuracy and sensitivity. The luminescence behavior observed in SAO:Fe^{3+} samples aligns well with the specific requirements of the LIR method. To evaluate this application potential, the temperature-dependent LIR of the 812 nm and 752 nm peaks under 285 nm excitation was extracted and plotted in Fig. 8(a). The data can be accurately fitted using the equation:

$$LIR = \frac{I_{812\ nm}}{I_{752\ nm}} \approx A exp\left(-\frac{\Delta E}{k_B T}\right) + B = 863956.76\ exp\left(\frac{-4663.69}{T}\right) + 0.92 \quad (3)$$

Here, $I_{812\ nm}$ and $I_{752\ nm}$ represent the emission peak intensity of the SAO:0.3 %Fe^{3+} sample at 812 nm and 752 nm, respectively. A and B are the fitting constants. The fitting curve denoted as the purple line, closely aligns with all experimental data points, labeled as green circles, demonstrating that the fitting model effectively reproduces the experimental results. Based on the fitted equation, the absolute temperature sensitivity S_a and the relative temperature sensitivity S_r were further derived using the following formulas and the results are shown in Fig. 8 (b):

$$S_a = \left|\frac{dLIR}{dT}\right| \quad (4)$$

$$S_r = \left|\frac{1}{LIR}\frac{dLIR}{dT}\right| \times 100\ \% \quad (5)$$

The maximum values of these two parameters in the temperature range considered in this work is 0.23 K^{-1} (S_a) and 2.72 % K^{-1} (S_r), respectively. The novel material we designed has comparable temperature sensitivities with phosphor reported in literature [2,3,37], indicating its promise as a luminescent temperature measurement material.

3.6. Encryption anti-counterfeiting of SAO:Fe^{3+}, Mn^{4+}

The SAO host material doped with Fe^{3+} exhibits two near-infrared emission peaks at 752 nm and 812 nm. The unintentionally doped Mn^{4+} ions as impurity in the starting material, Al_2O_3, suggests that co-doping with Mn^{4+} could further enrich the emission modes of SAO, as each emission exhibits distinct excitation behavior, as confirmed by intentional doping with Mn^{4+} [18] in Fig. 9(a).

Utilizing these three emission modes, we propose a conceptual scheme for encryption and anti-counterfeiting design. As illustrated in Fig. 9(b), when excited by 260, 285, 326 and 360 nm radiations, the sample exhibits various emission combinations from Fe^{3+} ions at tetrahedral and octahedral sites, along with Mn^{4+} ions. For instance, under 260 nm excitation, the emission spectrum displays peaks at 752 and 812 nm from Fe^{3+} ions at tetrahedral and octahedral sites, while 285 nm excitation additionally reveals the 655 nm emission peak from Mn^{4+}. This emission spectrum can be adjusted to a combination of the 655 nm and 812 nm peaks at 326 nm excitation, and to solely the 655 nm peak at 360 nm excitation.

These varying combinations offer substantial potential for encryption and anti-counterfeiting applications. For a simple demonstration, if we define the emission peaks at 655, 752 and 812 nm as "1″, "2″, and "3″, respectively, the emission spectra can be interpreted as "23″ or "123″ under 260 or 285 nm excitation, while the corresponding emissions at 326 or 360 nm excitation can be decoded as "13″ or "1″, respectively. Fig. 9(c) summarizes the corresponding coding and decoding method. This approach allows the luminescent material SAO:Fe^{3+}, Mn^{4+} to function as an anti-counterfeiting pigment. With a portable spectrometer, it can quickly identify and authenticate, significantly enhancing the

anti-counterfeiting capability of products. The analysis above demonstrates that SAO:Fe^{3+} luminescent material has promising application potential in the field of anti-counterfeiting. Furthermore, the distinct excitation-dependent intensities of these three emission centers suggest the potential for even more sophisticated, continuous-variable encryption schemes based on luminescence intensity ratios, which is a promising direction for future development.

4. Conclusion

In this study, we have successfully demonstrated the potential of Fe^{3+}-doped $Sr_4Al_{14}O_{25}$ as a dual-mode near-infrared luminescence thermometer. Through a combination of experimental measurements and first-principles calculations, we confirmed that Fe^{3+} ions occupy both tetrahedral and octahedral sites within the SAO lattice, leading to distinct NIR emissions at 752 and 812 nm. The temperature-dependent fluorescence intensity ratio (FIR) of these emissions exhibits a high relative temperature sensitivity of 2.72 % K^{-1}, highlighting the material's potential for precision temperature sensing. Additionally, the material's unique emission characteristics suggest its application in anti-counterfeiting technologies, where it can serve as a multi-model encryption pigment. This work not only expands the fundamental understanding of Fe^{3+}-doped NIR emitting materials but also paves the way for their practical application in advanced optoelectronic devices, offering a significant advancement in the field of luminescence thermometry. Furthermore, the phosphors developed in this work emitting within the 740–840 nm band demonstrate promising potential as illumination sources for machine vision cameras in expressway data acquisition systems, owing to their good low-light imaging capabilities.

CRediT authorship contribution statement

Bingyan Qu: Writing – review & editing, Writing – original draft, Software, Investigation, Formal analysis, Data curation. **Jindong Ni:** Writing – original draft, Investigation, Formal analysis, Data curation. **Chenglan Huang:** Formal analysis. **Junxiang Ding:** Data curation. **Rulong Zhou:** Software. **Caiping Zhu:** Funding acquisition. **Lei Wang *:** Writing – review & editing, Writing – original draft, Supervision, Methodology, Funding acquisition, Formal analysis, Conceptualization. **Hubertus T. Hintzen:** Writing – review & editing, Supervision, Formal analysis.

Declaration of competing interest

The authors declare that they have no known competing financial interests or personal relationships that could have appeared to influence the work reported in this paper.

Acknowledgments

This work is supported by the National Natural Science Foundation of China (Grant 52372143), Structural Material Innovation for Expressway Median Barrier Panels (W2025JSKF0291), the Industrial Innovation Guidance Fund of Tongcheng City & Hefei University of Technology (JZ2022YDZJ0083) and the Fundamental Research Funds for the Central Universities (PA2022GDGP0029, PA2023GDGP0042). The numerical calculations in this paper were done at the computing platforms of the High Performance Computing Center of Hefei University of Technology.

Appendix A. Supplementary data

Supplementary data to this article can be found online at https://doi.org/10.1016/j.ceramint.2025.12.297.

Data availability

The data supporting this article have been included as part of the Supplementary Information.

References

[1] S.C. Long, et al., Achieving high sensing sensitivity in a Dy^{3+} doped garnet phosphor toward optical thermometry, J. Mater. Chem. C 12 (2024) 19536–19544.
[2] Q. Wang, et al., A review on fluorescence intensity ratio thermometer based on rare-earth and transition metal ions doped inorganic luminescent materials, J. Alloys Compd. (2021) 850.
[3] L.A. Ramolise, et al., Recent advances on visible and near-infrared thermometric phosphors with ambient temperature sensitivity: a review, Coord. Chem. Rev. (2025) 522.
[4] D.Q. Chen, et al., Dual-activator luminescence of RE/TM:$Y_3Al_5O_{12}$ (RE = Eu^{3+}, Tb^{3+}, Dy^{3+}; TM = Mn^{4+}, Cr^{3+}) phosphors for self-referencing optical thermometry, J. Mater. Chem. C 4 (38) (2016) 9044–9051.
[5] Kiran, Y. Dwivedi, Temperature responsive behaviour of $SrAl_2O_4$(Eu, Dy): $ZnGa_2O_4$(Cr) phosphor-glass composite, Mater. Res. Bull. 182 (2025).
[6] H. Suo, et al., Ultra-sensitive optical nano-thermometer $LaPO_4$: Yb^{3+}/Nd^{3+} based on thermo-enhanced NIR-to-NIR emissions, Chem. Eng. J. 389 (2020).
[7] C. Matuszewska, K. Elzbieciak-Piecka, L. Marciniak, Transition metal ion-based nanocrystalline luminescent thermometry in $SrTiO_3$:Ni^{2+},Er^{3+} nanocrystals operating in the second optical window of biological tissues, J. Phys. Chem. C 123 (30) (2019) 18646–18653.
[8] D.P. Wang, et al., Achieving flat ultra-broadband NIR emission in Cr^{3+} doped garnet-type phosphors enabled by structural regulation toward multi-functional spectroscopy applications, Laser Photon. Rev. 19 (4) (2025) 202401256.
[9] H.Y. Lv, et al., Improved thermal stability of the near-infrared Al-modulated $Zn_3Ga_2GeO_8$: Cr^{3+} phosphors for plant growth applications, J. Am. Ceram. Soc. 105 (2) (2022) 966–976.
[10] L.T. Lin, et al., Trace impurity matters: origin and modulation of near-infrared luminescence in stannates, Chem. Mater. 36 (21) (2024) 10895–10901.
[11] C.N. Xie, et al., Fe^{3+}-doped broadband near-infrared phosphor with high quantum efficiency toward multifunctional pc-LEDs applications, J. Alloys Compd. (2024) 1007.
[12] W.M. Piotrowski, et al., Improving the luminescent properties of Fe^{3+} in $CaAl_4O_7$ by co-doping with Bi^{3+} ions, Mater. Res. Bull. 181 (2025).
[13] F.Q. He, E.H. Song, Q.Y. Zhang, Energy transfer-induced blue light-excited broadband near-infrared luminescence in fluoride Na_3AlF_6:Mn^{4+},Fe^{3+}, J. Mater. Chem. C 12 (37) (2024) 15137–15143.
[14] J. Ni, et al., The experimental and theoretical research on the near infrared luminescent property of $KAl_{11}O_{17}$:Fe^{3+} and $RbAl_{11}O_{17}$:Fe^{3+}, Opt. Mater. X 16 (2022), 100212-100212.
[15] M. Wu, et al., Double-site emission of Eu^{2+} ions in $Sr_4Al_{14}O_{25}$: Eu^{2+} phosphors for self-calibrated optical thermometry, Opt. Mater. 88 (2019) 704–710.
[16] P. Du, et al., Multi-site occupancies and photoluminescence characteristics in developed Eu^{2+}-activated $Ba_5SiO_4Cl_6$ bifunctional platform: towards manufacturable optical thermometer and indoor illumination, J. Alloys Compd. (2020) 826.
[17] Y.Z. Liu, et al., $Sr_4Al_{14}O_{25}$:Li^{+},Mn^{4+} phosphor-in-glass film: erosion behavior and luminescence property, Dalton Trans. 53 (37) (2024) 15471–15480.
[18] Y.D. Xu, et al., Preparation and luminescent properties of a new red phosphor ($Sr_4Al_{14}O_{25}$:Mn^{4+}) for white LEDs, J. Alloys Compd. 550 (2013) 226–230.
[19] W.Z. Sun, et al., Bright yellow-emitting long persistent luminescence from Mn^{2+}-activated strontium aluminate phosphor, J. Rare Earths 40 (7) (2022) 1029–1036.
[20] E. Jara, et al., Optical spectroscopy of the $Sr_4Al_{14}O_{25}$:Mn^{4+},Cr^{3+} phosphor: pressure and temperature dependences, J. Mater. Chem. C 10 (16) (2022) 6380–6391.
[21] Kresse, Hafner, Ab initio molecular dynamics for liquid metals, Phys. Rev. B 47 (1) (1993) 558–561.
[22] Kresse, Furthmuller, Efficient iterative schemes for ab initio total-energy calculations using a plane-wave basis set, Phys. Rev. B 54 (16) (1996) 11169–11186.
[23] P. John, K.B. Perdew, Matthias Ernzerhof, Generalized gradient approximation made simple, Phys. Rev. Lett. 77 (18) (1996) 3865–3868.
[24] S.L. Dudarev, et al., Electron-energy-loss spectra and the structural stability of nickel oxide: an LSDA+U study, Physical Review B (Condensed Matter) 57 (3) (1998) 1505–1509.
[25] C.G. Van de Walle, J. Neugebauer, First-principles calculations for defects and impurities: applications to III-nitrides, J. Appl. Phys. 95 (8) (2004) 3851–3879.
[26] R.D. Shannon, Revised effective ionic radii and systematic studies of interatomic distances in halides and chalcogenides, Acta Crystallographica, Section A (Crystal Physics, Diffraction, Theoretical and General Crystallography) A32 (5) (1976) 751–767.
[27] D. Dutczak, et al., Eu^{2+} luminescence in strontium aluminates, Phys. Chem. Chem. Phys. 17 (23) (2015) 15236–15249.
[28] B.Y. Qu, et al., The predictability of the ground state of $3d^n$ transition metal ion as luminescent centers in the tetrahedral sites in inorganic compounds, J. Lumin. 247 (2022) 118919.
[29] L. Wang, et al., Quantitative insights into the chemical trend of four-coordinated Mn^{2+} emission in inorganic compounds, J. Lumin. 225 (2020) 117399.

[30] L. Wang, et al., Understanding the quenching nature of Mn^{4+} in wide band gap inorganic compounds: design principles for Mn^{4+} phosphors with higher efficiency, Phys. Chem. Chem. Phys. 20 (25) (2018) 16992–16999.
[31] Y.L. Ye, et al., Boosting near-infrared emission in spinel-type phosphor via oxygen vacancy engineering for versatile application, Adv. Funct. Mater. 34 (42) (2024) 2405048.
[32] K. Kniec, et al., $LiAl_5O_8:Fe^{3+}$ and $LiAl_5O_8:Fe^{3+}$, Nd^{3+} as a new luminescent nanothermometer operating in 1st biological optical window, Nanomaterials 10 (2) (2020).
[33] C.J. Duan, A.C.A. Delsing, H.T. Hintzen, Red emission from Mn^{2+} on a tetrahedral site in $MgSiN_2$, J. Lumin. 129 (6) (2009) 645–649.
[34] L.Q. Yan, et al., Emerging Fe^{3+} doped broad NIR-Emitting phosphor $Ca_{2.5}Hf_{2.5}(Ga, Al)_3O_{12}$: Fe^{3+} for LWUV pumped NIR LED, Laser Photon. Rev. 18 (5) (2024).
[35] F.Y. Zhao, et al., Structural confinement toward suppressing concentration and thermal quenching for improving near-infrared luminescence of Fe^{3+}, Inorg. Chem. Front. 10 (22) (2023) 6701–6710.
[36] X. Chen, Z. Xia, Luminescence properties of $Li_2Ca_2ScV_3O_{12}$ and $Li_2Ca_2ScV_3O_{12}:Eu^{3+}$ Synthesized by solid-state reaction method, Opt. Mater. 35 (12) (2013) 2736–2739.
[37] M.J. Song, et al., Spectroscopic and temperature sensing properties of Sm^{3+} in self-activated $CsLu(WO_4)_2$ phosphors, J. Rare Earths 42 (11) (2024) 2033–2042.